Kobe University Repository : Kernel

PDF issue: 2025-12-05

Evaluation and design of a large-scale cloaking device by the Hamiltonian-based ray-tracing method. Part I: full-mesh representation

Tanaka, Tatsuo

Matoba, Osamu

(Citation)
Journal of the Optical Society of America B,34(5):1041-1051

(Issue Date)
2017-05-01

(Resource Type)
journal article

(Version)
Accepted Manuscript

(Rights)
© 2017 Optical Society of America

(URL)
https://hdl.handle.net/20.500.14094/90006441

Evaluation and design of a large-scale cloaking device by Hamiltonian-based ray-tracing method. Part I: Full-mesh representation

Tatsuo Tanaka,[1,2,*] Osamu Matoba[1]

[1]*Deparrtment of Systems Science, Graduate School of System Informatics, Kobe University, Rokkodai 1-1, Nada, Kobe 657-8501, Japan*
[2]*Computer Aided Engineering Dept., Production Technology Center, Corporate Production Technology, Asahi Kasei Corporation, 1-3-2, Yakoh, Kawasaki, Kawasaki, Kanagawa 210-0863, Japan*
**Corresponding author: tanaka.tdn@om.asahi-kasei.co.jp*

Received XX Month XXXX; revised XX Month, XXXX; accepted XX Month XXXX; posted XX Month XXXX (Doc. ID XXXXX); published XX Month XXXX

A Hamiltonian-based ray tracing technique is applied to the evaluation of the performance of cloaking devices with arbitrary shapes based on full-mesh representation. The constitutive parameters of cloaking devices are calculated by the finite element method. The cloaking characteristics of a double cylindrical cloaking device and a huge cloaking device with completely arbitrary shape are evaluated. The numerical results showed that fine mesh structure is required for better cloaking performance. The full-mesh representation is useful for fabrication design.

© 2017 Optical Society of America

OCIS codes: *(230.3205) Invisibility cloaks; (080.2710) Inhomogeneous optical media; (080.2740) Geometric optical design; (080.5692) Ray trajectories in inhomogeneous media; (160.3918) Metamaterials.*

http://dx.doi.org/10.1364/AO.99.099999

1. Introduction

Cloaking phenomena are very attractive because light is guided around hidden objects, and it emerges as if the hidden objects do not exist [1-4]. Recently, theoretical works based on transformation optics [1,2] have been proposed and then realistic engineering applications can be expected. Furthermore, based on force-loaded transformation optics, force-induced transformational devices, such as an optical escalator, have been proposed [5].

Invisibility cloaking enables many industrial uses. For example, transparent pillars of automobile bodies are expected to reduce a dead zone in the view field of a driver. It leads to the decline of the number of car accidents [6-8]. In the medical field, the usability of the operator will be improved if the hands of surgery-supporting robots can be a transparent medium [9]. For such engineering applications, large-scale cloaking devices are required. Full-mesh representation is also required for the fabrication.

So far various cloaking devices with not only regular shapes such as sphere, cylinder, and cone [10, 11] but also arbitrary shapes [12–16] have been designed. For ideal cases, the cloaking effects are verified based on full-wave simulations. However, it is difficult to apply full-wave simulations because of the lack of computational memory capacity to verify the cloaking effects for large-scale objects. As one of the possible candidates for methods to evaluate the cloaking effects for large-scale objects, Hamiltonian-based ray tracing [17–22] has been proposed. This method can handle mediums with anisotropy and inhomogeneity in their constitutive parameters, which are characteristics of the cloaking devices derived by transformation optics.

Additionally, the Hamiltonian-based ray tracing has been extended to arbitrary coordinate systems and curved spaces [23]. Besides cloaking devices, an Eaton lens [23] and a graded negative-index metamaterial magnifier [24] have been investigated by this method. Recently, a method called "force tracing" to trace the optical force has been proposed based on the Hamiltonian-based ray tracing [25].

In order to deal with cloaking devices with arbitrary large-scale shapes, two problems have to be solved. One is how to represent the surface of cloaking devices. In our previous study [26], we proposed a Hamiltonian-based ray-tracing method adapting a mesh representation approach, where the surfaces of arbitrary shapes are modeled by the mesh structure as shown in Fig. 1 (a). The other problem is how to determine the constitutive parameters of cloaking devices with arbitrary shapes. This problem can be solved by the numerical modeling of the constitutive parameters based on the finite element method (FEM) proposed in [27].

In this paper, we apply the Hamiltonian ray tracing to a large-scale object with a full-mesh representation approach, where both the surface and the inner area of a cloaking device are represented by the mesh structure based on the finite element method (FEM) as shown in Fig. 1(b). The cloaking performance of cloaking devices with the full-mesh representation is evaluated by comparing it with that with the mesh representation for the surface and the analytical distribution inside the device.

The rest of the paper is organized as follows. In CHAPTER 2, we describe the computational method of our Hamiltonian ray tracing as well as the numerical method of the constitutive parameters of the cloaking devices. In CHAPTER 3, we present the determination of the mesh resolution of the surface and the inner area of a cloaking device. In addition, the numerical analyses of a double cylindrical cloaking device and a huge cloaking device with a more complicated shape are presented.

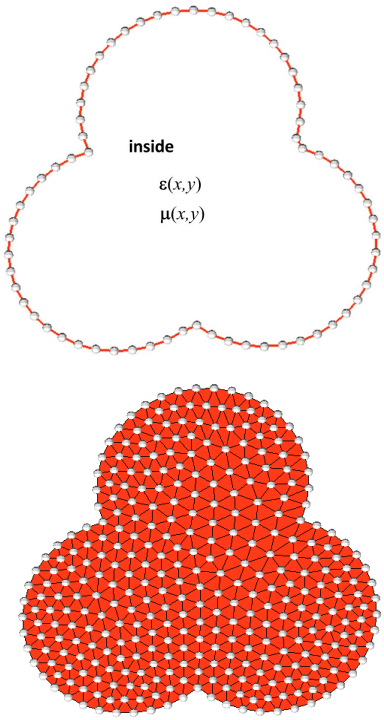

Fig. 1. (a) The example of linear mesh structure that represent the surface of the cloaking device. (b) The example of triangular mesh structure inside of the cloaking device.

2. Full-mesh Representation of Cloaking Device and Evaluation Method

We briefly describe the Hamiltonian-based ray tracing as described in [10, 26] in 2.1. Next, the calculation method of relative permittivity tensor and permeability tensor is described for the full-mesh representation in 2.2. The evaluation method of cloaking performance is described in 2.3.

2.1. Hamiltonian-based ray tracing

As described in Refs. 10 and 26, we assume that the cloaking media are impedance-matched with the surrounding medium, i.e., $\boldsymbol{\varepsilon}=\boldsymbol{\mu}=\mathbf{n}$, where $\boldsymbol{\varepsilon}$ and $\boldsymbol{\mu}$ are relative permittivity tensor and relative permeability tensor of the cloaking medium. Then, the Hamiltonian of the cloaking medium can be defined as

$$H = \boldsymbol{k}^{T} \cdot \mathbf{n} \cdot \boldsymbol{k} - \det(\mathbf{n}), \tag{1}$$

where $\boldsymbol{k}$ is the wave vector inside the cloaking medium. A ray path can be obtained by solving the pair of coupled, first order ordinary differential ray equations,

$$\frac{\partial \boldsymbol{r}}{\partial \tau} = \frac{\partial H}{\partial \boldsymbol{k}}, \tag{2a}$$

$$\frac{\partial \boldsymbol{k}}{\partial \tau} = -\frac{\partial H}{\partial \boldsymbol{r}}, \tag{2b}$$

where τ parameterizes the ray path and $\boldsymbol{r}$ is the position vector of the ray.

2.2. Calculation of Relative Permittivity Tensor and Permeability Tensor

We consider the space transformation from the original space, $\boldsymbol{r}=(x,y,z)$, to the transformed space, $\boldsymbol{r}'=(x',y',z')$, as shown in Fig. 2 [26]. According to transformation optics, the relative permittivity tensor and the permeability tensor in the transformed space, $\boldsymbol{\varepsilon}'$ and $\boldsymbol{\mu}'$, are obtained as

$$\boldsymbol{\varepsilon}' = \frac{\mathbf{A} \cdot \boldsymbol{\varepsilon} \cdot \mathbf{A}^{T}}{\det(\mathbf{A})}, \tag{3}$$

$$\boldsymbol{\mu}' = \frac{\mathbf{A} \cdot \boldsymbol{\mu} \cdot \mathbf{A}^{T}}{\det(\mathbf{A})}, \tag{4}$$

where $\boldsymbol{\varepsilon}$ and $\boldsymbol{\mu}$ denote the relative permittivity tensor and the permeability tensor in the original space. $\mathbf{A}$ is the Jacobian transformation matrix defined as

$$\mathbf{A} = \begin{pmatrix} \partial x'/\partial x & \partial x'/\partial y & \partial x'/\partial z \\ \partial y'/\partial x & \partial y'/\partial y & \partial y'/\partial z \\ \partial z'/\partial x & \partial z'/\partial y & \partial z'/\partial z \end{pmatrix}, \tag{5}$$

Therefore, $\boldsymbol{\varepsilon}'$ and $\boldsymbol{\mu}'$ can be calculated if the components of $\mathbf{A}$ are obtained.

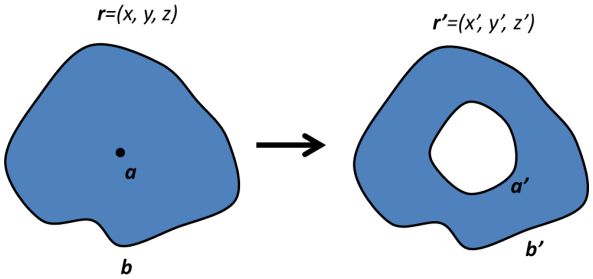

Fig. 2. The space transformation from the original space, $\boldsymbol{r}=(x,y,z)$, to the transformed space, $\boldsymbol{r}'=(x',y',z')$.

Next, we consider the calculation of the components of $\mathbf{A}$. If the transformed coordinate, $\boldsymbol{r}'=(x',y',z')$, can be described as analytical functions of the components of $\boldsymbol{r}$, that is, x, y or z, the components of $\mathbf{A}$

can also be obtained analytically, which leads to the analytical solutions of $\boldsymbol{\varepsilon}'$ and $\boldsymbol{\mu}'$.

For example, in the case of cylinder cloaking with the rotational symmetry axis aligned along the z-axis [10], we choose

$$\boldsymbol{\varepsilon}' = \boldsymbol{\mu}' = \mathbf{n}' = \frac{\rho}{\rho - a}\mathbf{T} - \frac{2a\rho - a^2}{\rho^3(\rho - a)}\boldsymbol{\rho} \otimes \boldsymbol{\rho} + \left(\frac{b}{b-a}\right)^2 \frac{\rho - a}{\rho}\mathbf{Z}, \tag{6}$$

where $\boldsymbol{\rho}=(x', y', 0)$ where we set the coordinate origin to the center of the cloaking device, ρ is the magnitude of $\boldsymbol{\rho}$, a and b are the inner radius and the outer radius of the cylindrical shell, respectively, $\mathbf{T}$ and $\mathbf{Z}$ are the following matrixes.

$$\mathbf{T} = \begin{pmatrix} 1 & 0 & 0 \\ 0 & 1 & 0 \\ 0 & 0 & 0 \end{pmatrix}, \tag{7}$$

$$\mathbf{Z} = \begin{pmatrix} 0 & 0 & 0 \\ 0 & 0 & 0 \\ 0 & 0 & 1 \end{pmatrix}, \tag{8}$$

On the other hand, for cloaking devices with arbitrary shapes, it is difficult to describe $\boldsymbol{r}'$ as analytical functions of the components of $\boldsymbol{r}$, as well as $\boldsymbol{\varepsilon}'$ and $\boldsymbol{\mu}'$. In order to solve the problem, the numerical method for calculation of the relative permittivity tensor and permeability tensor of a cloaking device has been proposed [27]. We briefly describe the method as described in [27].

The space transformation as shown in Fig. 2 can be assumed to be a forced deformation problem in the continuum mechanics. Therefore, the transformed coordinates are expressed as follows,

$$\begin{pmatrix} x' \\ y' \\ z' \end{pmatrix} = \begin{pmatrix} x \\ y \\ z \end{pmatrix} + \begin{pmatrix} U_x \\ U_y \\ U_z \end{pmatrix}, \tag{9}$$

where U_i (i=x,y,z) are called the displacement field in the continuum mechanics. Hence, the components of $\mathbf{A}$, can be expressed as

$$\begin{aligned} \mathbf{A} &= \begin{pmatrix} 1+\partial U_x/\partial x & \partial U_x/\partial y & \partial U_x/\partial z \\ \partial U_y/\partial x & 1+\partial U_y/\partial y & \partial U_y/\partial z \\ \partial U_z/\partial x & \partial U_z/\partial y & 1+\partial U_z/\partial z \end{pmatrix} \\ &= \begin{pmatrix} 1 & 0 & 0 \\ 0 & 1 & 0 \\ 0 & 0 & 1 \end{pmatrix} + \begin{pmatrix} \partial U_x/\partial x & \partial U_x/\partial y & \partial U_x/\partial z \\ \partial U_y/\partial x & \partial U_y/\partial y & \partial U_y/\partial z \\ \partial U_z/\partial x & \partial U_z/\partial y & \partial U_z/\partial z \end{pmatrix} \\ &= \mathbf{I} + \mathbf{G}, \end{aligned} \tag{10}$$

where the tensor $\mathbf{G}$ is called the deformation gradient tensor in the continuum mechanics.

Figure 2 indicates that the outer boundary of the transformed region, $\boldsymbol{b}'$, is the same as that of the original region, $\boldsymbol{b}$. On the other hand, the inner boundary of the transformed region, $\boldsymbol{a}'$, is extended from the point of the original region, $\boldsymbol{a}$. Therefore, the boundary conditions for the forced deformation problem are derived as

$$\begin{pmatrix} U_x(\boldsymbol{r_b}) \\ U_y(\boldsymbol{r_b}) \\ U_z(\boldsymbol{r_b}) \end{pmatrix} = \begin{pmatrix} 0 \\ 0 \\ 0 \end{pmatrix}, \tag{11}$$

$$\begin{pmatrix} U_x(\boldsymbol{r_a}) \\ U_y(\boldsymbol{r_a}) \\ U_z(\boldsymbol{r_a}) \end{pmatrix} = \boldsymbol{r}'_a - \boldsymbol{r}_a = \begin{pmatrix} x'_a - x_a \\ x'_a - x_a \\ x'_a - x_a \end{pmatrix} = \begin{pmatrix} x'_a \\ x'_a \\ x'_a \end{pmatrix}, \tag{12}$$

where $\boldsymbol{r_a} = (x_a, y_a, z_a) = (0, 0, 0)$ and $\boldsymbol{r_b} = (x_b, y_b, z_b)$ are position vectors at the point, $\boldsymbol{a}$ and the outer boundary of the original region, $\boldsymbol{b}$, and $\boldsymbol{r'_a} = (x'_a, y'_a, z'_a)$ is a position vector at the inner boundary of the transformed region, $\boldsymbol{a}'$.

The displacement field and the deformation gradient tensor can be calculated by solving the Laplace's equation as,

$$\left(\frac{\partial^2}{\partial x^2} + \frac{\partial^2}{\partial y^2} + \frac{\partial^2}{\partial z^2}\right) U_i = 0, \quad (i = x, y, z), \tag{13}$$

with the Dirichlet boundary conditions as shown in Eqs. (11) and (12).

However, the solution of the Laplace's equation, Eq. (13), becomes singular at the point $\boldsymbol{a}$. In order to keep from the singular solution, the inverse transformation, $\boldsymbol{r}' \rightarrow \boldsymbol{r}$, is considered, where the original coordinates are expressed as follows,

$$\begin{pmatrix} x \\ y \\ z \end{pmatrix} = \begin{pmatrix} x' \\ y' \\ z' \end{pmatrix} + \begin{pmatrix} U'_x \\ U'_y \\ U'_z \end{pmatrix}, \tag{14}$$

where U'_i (i=x,y,z) are the displacement fields. Then we obtain the inverse form of the Laplace's equation as

$$\left(\frac{\partial^2}{\partial x'^2} + \frac{\partial^2}{\partial y'^2} + \frac{\partial^2}{\partial z'^2}\right) U'_i = 0, \quad (i = x, y, z), \tag{15}$$

The Dirichlet boundary conditions correspondingly become

$$\begin{pmatrix} U'_x(\boldsymbol{r'_b}) \\ U'_y(\boldsymbol{r'_b}) \\ U'_z(\boldsymbol{r'_b}) \end{pmatrix} = \begin{pmatrix} 0 \\ 0 \\ 0 \end{pmatrix}, \tag{16}$$

$$\begin{pmatrix} U'_x(\boldsymbol{r'_a}) \\ U'_y(\boldsymbol{r'_a}) \\ U'_z(\boldsymbol{r'_a}) \end{pmatrix} = \boldsymbol{r}_a - \boldsymbol{r}'_a = \begin{pmatrix} x_a - x'_a \\ y_a - y'_a \\ z_a - z'_a \end{pmatrix} = \begin{pmatrix} -x'_a \\ -y'_a \\ -z'_a \end{pmatrix}, \tag{17}$$

where $\boldsymbol{r'_b} = (x'_b, y'_b, z'_b)$ is a position vector at the outer boundary of the transformed region, $\boldsymbol{b}'$.

By solving the Eqs. (15), (16) and (17), the deformation gradient tensor can be obtained as follow,

$$\mathbf{G'} = \begin{pmatrix} \partial U'_x/\partial x' & \partial U'_x/\partial y' & \partial U'_x/\partial z' \\ \partial U'_y/\partial x' & \partial U'_y/\partial y' & \partial U'_y/\partial z' \\ \partial U'_z/\partial x' & \partial U'_z/\partial y' & \partial U'_z/\partial z' \end{pmatrix}, \quad (18)$$

From the components of **G'**, we can calculate the components of the Jacobian transformation matrix of the inverse transformation as follows,

$$\mathbf{A'} = \begin{pmatrix} \partial x/\partial x' & \partial x/\partial y' & \partial x/\partial z' \\ \partial y/\partial x' & \partial y/\partial y' & \partial y/\partial z' \\ \partial z/\partial x' & \partial z/\partial y' & \partial z/\partial z' \end{pmatrix}$$

$$= \begin{pmatrix} 1+\partial U'_x/\partial x' & \partial U'_x/\partial y' & \partial U'_x/\partial z' \\ \partial U'_y/\partial x' & 1+\partial U'_y/\partial y' & \partial U'_y/\partial z' \\ \partial U'_z/\partial x' & \partial U'_z/\partial y' & 1+\partial U'_z/\partial z' \end{pmatrix}$$

$$= \mathbf{I} + \mathbf{G'}, \quad (19)$$

A can be obtained by the inversion of **A'**. Finally, **ε'** and **μ'** are obtained by applying **A** into Eqs. (3) and (4), respectively.

The solution of Laplace's equation was achieved based on the FEM by employing the open source software, Elmer from CSC [28].

Since the FEM-based solutions for **ε'** and **μ'** are discretized in triangular meshes inside of the cloaking device, interpolation of **ε'** and **μ'** are necessary for the Hamiltonian-based ray tracing. In this paper, **ε'** and **μ'** are expressed as linear functions of the components of a position vector inside each element used for the solution of the Laplace's equation.

Since space transformations can be defined for cloaking devices with arbitrary shapes, **ε'** and **μ'** of the cloaking devices can be obtained from transformation optics [29]. Therefore, the numerical modeling of **ε'** and **μ'** based on the FEM described above can be also applied to cloaking devices with arbitrary shapes including irregular shapes [14, 16, 30, 31]. Nevertheless, we need to pay attention to the accuracy of the solution from the FEM since it determines the accuracy of **ε'** and **μ'**, which affects the performance of cloaking devices.

2.3. Evaluation Method of the Performance of Cloaking Device

A calculation model is illustrated in Fig. 3. One hundred rays are radiated from the point put in front of the cloaking device, within an angle of view of 60°. If a ray enters the inner surface of the cloaking device, the ray is assumed to be absorbed by the surface. On the back of the cloaking device, the screen is placed for the measurement of the rays. When the cloaking is perfect, each position of the intersections of the rays and the screen is the same as that without the cloaking device. On the other hand, when a ray does not reach the screen or the intersection position is different from the expected position, it shows deteriorated performance.

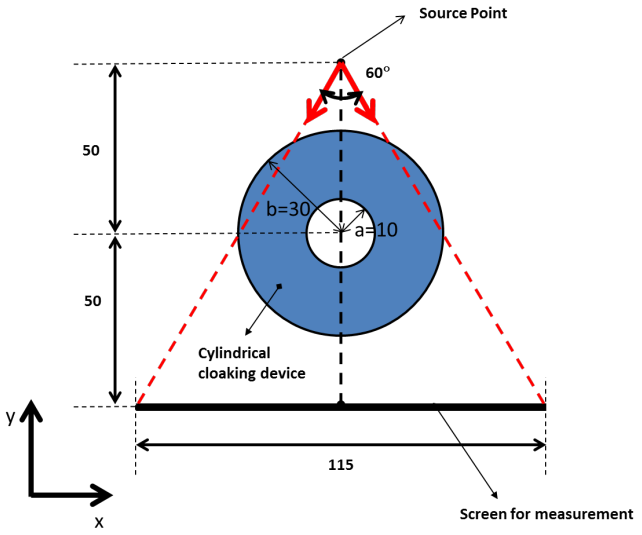

Fig. 3. Calculation model for the cylindrical cloaking device

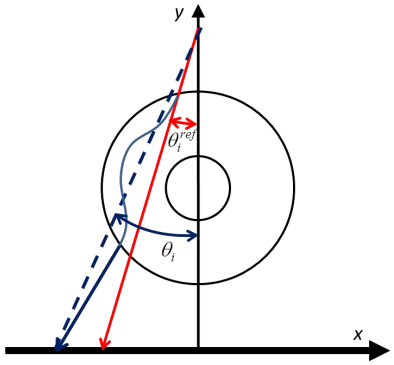

Fig. 4. The angle for the evaluation of cloaking performance. The red solid arrow corresponds to the ray trajectory without the cloaking device. The blue solid arrow corresponds to the ray trajectory with the cloaking device. The blue dashed line is the straight line passing the source point and the intersection between the ray trajectory and the screen.

For the evaluation of cloaking performance, we consider the angle between the straight line passing the source point and the intersection, and the y axis as shown in Fig. 4. As a performance index, we calculate the mean square root of the difference between the angles with the cloaking device and without the cloaking device as follows,

$$\Delta\theta = \sqrt{\frac{\sum_{i}^{N_{ray}} \left(\theta_i - \theta_i^{ref}\right)^2}{N_{ray}}}, \quad (20)$$

where i is the index of a ray, θ_i and θ^{ref}_i are the angle with the cloaking device and without the cloaking device, respectively, N_{ray} is the number of the total rays. N_{ray} is set to be 100. If the value of $\theta_i - \theta^{ref}_i$ becomes outside the range $-30 < \theta_i - \theta^{ref}_i < 30$ or the ray doesn't reach the screen, we set that $|\theta_i - \theta^{ref}_i| = 30°$. Perfect cloaking is obtained when the value of $\Delta\theta$ equals to 0.0°. On the other hand, the increase of the value of $\Delta\theta$ shows the deterioration of the performance of the cloaking device.

The dependence of cloaking performance on the radiation angle is evaluated as,

$$\Delta\theta_i = \theta_i - \theta_i^{ref} \quad . \qquad (21)$$

In order to design a cloaking device for a large-scale object, such as pillars of automobile bodies and surgery support robots, where it is difficult to apply full-wave simulations in terms of computational resources, the geometrical ray tracing was employed. In addition, since a medium of the cloaking device is inhomogeneous and anisotropic in their electric permittivity and magnetic permeability, the ray trajectories are calculated based on the Hamiltonian equations [10, 20, 21].

3. Numerical Results

3.1. Cloaking Performance of Mesh Representation of the Surface

In Ref. 26, we have proposed a method to analyze the cloaking performance based on a Hamiltonian-based ray-tracing method where the surfaces of cloaking devices with arbitrary shapes are represented by the mesh structure. The numerical results indicated that the mesh resolution of the surfaces contributes to cloaking performance. In this paper, the cloaking performance of a two-dimensional cylindrical cloaking device as shown in Fig. 3 with the full-mesh representation is evaluated. Here, ideal cloaking characteristic is presented by evaluating the cloaking performance of the cloaking device with the mesh representation of the surface and the rigorous distribution of $\boldsymbol{\varepsilon}$ and $\boldsymbol{\mu}$ inside the device. The results give us the ideal performance for the full-mesh representation in 3.2.

The cloaking performance of the cloaking device is evaluated by the mesh representation with five mesh resolutions where the average lengths are 2.5, 1.0, 0.5, 0.25, and 0.10 mm, as well as by the rigorous function approach, where the surface is modeled by rigorous functions. In both approaches, $\boldsymbol{\varepsilon}$ and $\boldsymbol{\mu}$ inside the cloaking device are assigned as the analytical functions of a position vector, $\boldsymbol{r}=(x,y)$, as shown in Eq. (6). Based on the result, we determine the mesh resolution of the surfaces of cloaking devices with arbitrary shapes.

Here, a relative mesh resolution is defined as the ratio of a mesh size to the size of the cloaking device so that it can be universally applied to any other structure. The relative mesh resolutions are 4.17e-02, 1.67e-02, 8.33e-03, 4.17e-03, and 1.67e-03 when the size of the cloaking device is 60 mm and the mesh sizes are 2.5, 1.0, 0.5, 0.25, and 0.10 mm, respectively. Hereafter, we investigate the numerical results based on the relative mesh resolution.

The ray paths without a cloaking device are shown in Fig. 5 (a), while those with the cloaking device obtained by the rigorous function approach are shown in Fig. 5 (b). We can find that the ray paths after passing through the cloaking device in Fig. 5 (a) and the corresponding ray paths in Fig. 5 (b) are almost the same. The dependence of the cloaking performance on the radiation angle for the rigorous function approach is shown in Fig. 6, suggesting that the cloaking performance gets deteriorated slightly at the radiation angles close to 0.0°. From Table 1, the value of $\Delta\theta$ for the rigorous function approach, $\Delta\theta$=7.90e-05°, is very close to 0.0°, which suggests that the almost perfect cloaking can be obtained by using the rigorous function approach for the representation of the surface and the analytical function approach for the representation of $\boldsymbol{\varepsilon}$ and $\boldsymbol{\mu}$.

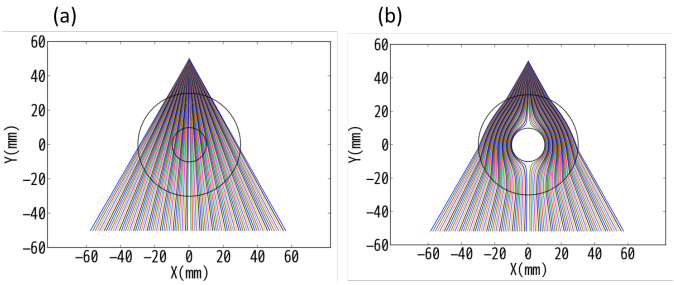

Fig. 5. (a) The ray paths without a cloaking device. (b) The ray paths with the cylindrical cloaking device calculated by the rigorous function approach for the surface of the cloaking device and the analytical function approach for $\boldsymbol{\varepsilon}$ and $\boldsymbol{\mu}$ inside of the cloaking device.

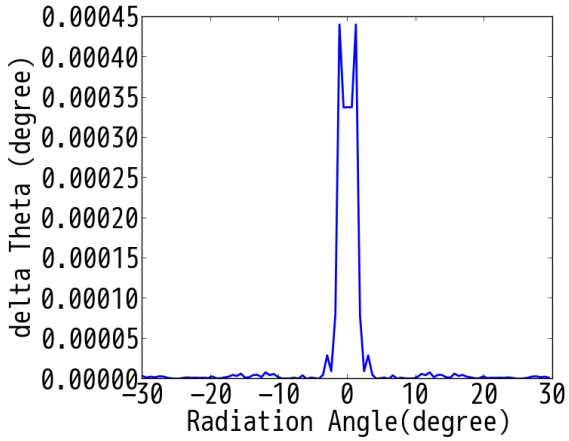

Fig. 6. The dependence of the cloaking performance on the radiation angle calculated by the rigorous function approach for the surface of the cloaking device and the analytical function approach for $\boldsymbol{\varepsilon}$ and $\boldsymbol{\mu}$ inside of the cloaking device.

The ray paths obtained by the mesh representation approach with five relative mesh resolutions are illustrated in Fig. 7 (a)-(e), respectively. From the results, the dependence of the performance on the relative mesh resolution of the surface of the cloaking device was calculated in Table 1. It shows that the performance becomes better as the relative mesh resolution gets finer.

The reason why the coarse relative mesh resolution showed the deteriorated performance is considered as follows. Since the normal vector of the surface in the mesh representation is slightly different from that in the rigorous function representation, the direction of the refracted ray in the mesh representation deviates from the correct direction. The error of the direction of the refracted ray causes the ray path to change, which leads to the deteriorated cloaking performance.

The dependence of the cloaking performance on the radiation angle for five relative mesh resolutions is shown in Figs. 8 (a)-(e), respectively. We can notice that the cloaking performance oscillates with the radiation angle. The amplitude and the period of the oscillation are decreased as the relative mesh resolution becomes finer. In order to explain the reason for the oscillation, we show two ray paths for the relative mesh resolution of 4.17e-02 in Fig. 9. The red path corresponding to the radiation angle of -27.9° yields deteriorated performance while the blue path corresponding to the radiation angle of -26.3° yields good performance. We can find the difference between the two paths in the position of the intersection of the ray and the surface. The red path intersects with the surface near the end of the mesh on the surface. In contrast, the blue path intersects with the surface at the middle of the mesh on the surface. If a ray intersects with

the surface near the end of the mesh, the difference of the normal vector of the surface in the mesh representation and that in the rigorous function representation can be seen to be large from the geometrical consideration as show in Fig. 9. The large difference of the normal vectors leads to deteriorate performance as mentioned above. On the other hand, if a ray intersects with the surface at the middle of the mesh, the difference can be small and it results in good performance. This suggests that the cloaking performance depends on the intersection position, which causes the oscillation with the radiation angle.

Here, we set a criterion for good cloaking performance as $\Delta\theta$=1.0°. From Table 1, we can find that the relative mesh resolution of the surface finer than 0.125 can satisfy the criterion.

Table 1: Performances of cylindrical cloaking calculated for the rigorous function approach and the mesh representation approach for the surface of the cloaking device

Number	Surface representation	Inside representation	$\Delta\theta$ (°)
1	Rigorous function	Analytical function	7.99e-05
2		Analytical function	5.86e-01
3		Analytical function	2.70e-01
4	Mesh	Analytical function	1.15e-01
5		Analytical function	5.60e-02
6		Analytical function	2.44e-02

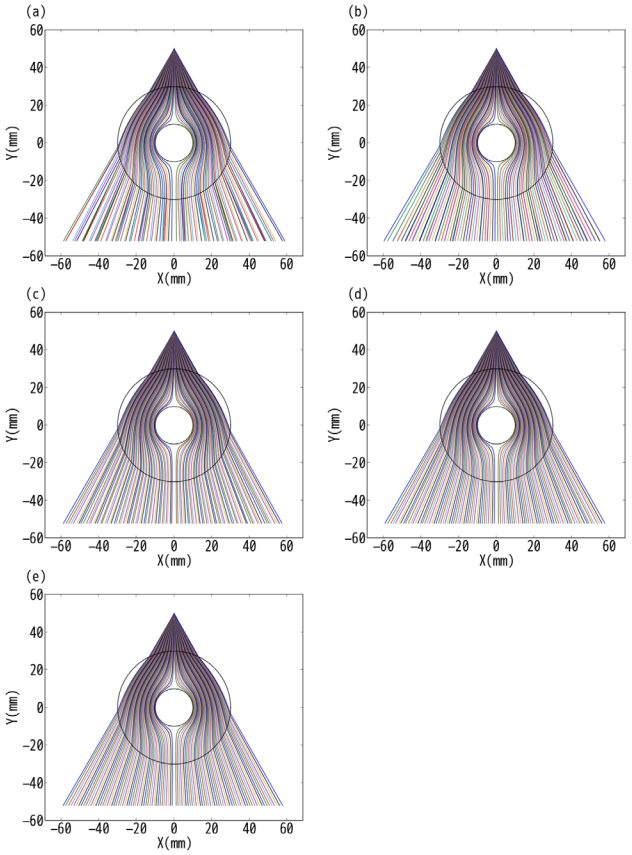

Fig. 7. The ray trajectories with the cylindrical cloaking device for the mesh representation approach for the surface of the cloaking device and the analytical function approach for ε and μ inside of the cloaking device. The relative mesh resolutions are (a) 4.17e-02, (b) 1.67e-02, (c) 8.33e-03, (d) 4.17e-03 and (e) 1.67e-03.

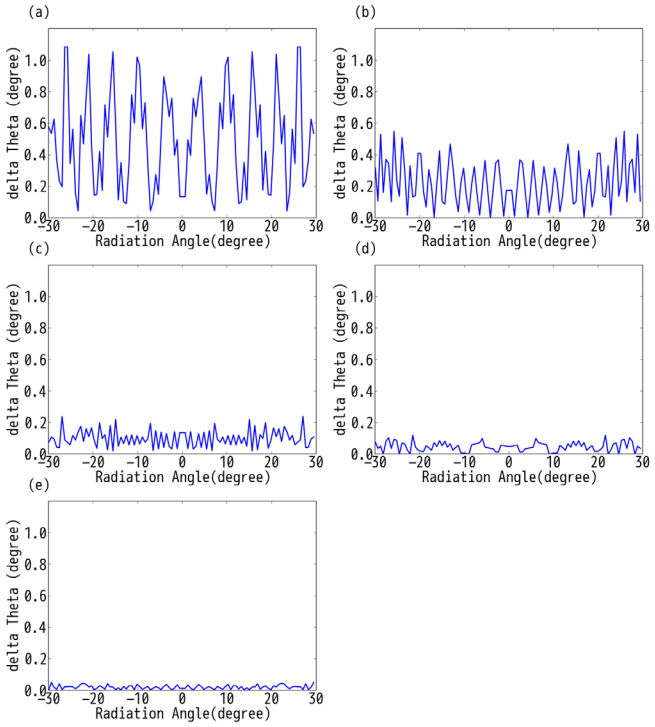

Fig. 8. The dependence of the cloaking performance of the cylindrical cloaking device on the radiation angle for the mesh representation approach for the surface of the cloaking device and the analytical function approach for ε and μ inside of the cloaking device. The relative mesh resolutions are (a) 4.17e-02, (b) 1.67e-02, (c) 8.33e-03, (d) 4.17e-03 and (e) 1.67e-03.

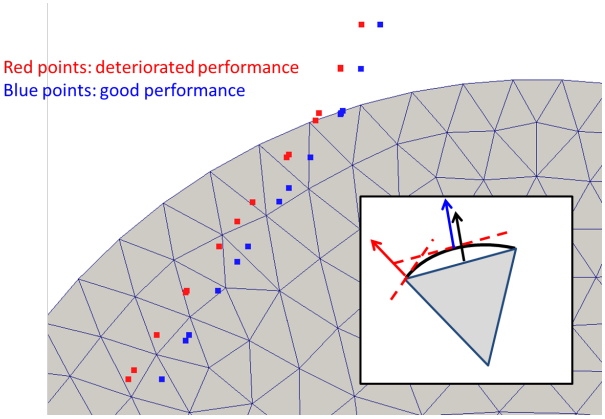

Fig. 9. The explanation for the oscillation of the perfomance with the radiation angle.

3.2. Cloaking Performance of Full-mesh Representation

Because the numerical method for the calculation of ε and μ described in 2.2 utilizes the solution of the Laplace's equation based on the FEM, the full-mesh resolution inside a cloaking device contributes the cloaking performance. Here, we investigate the dependence of the cloaking performance on the full-mesh resolution inside the cloaking device. Based on the result, we determine the full-mesh resolution inside cloaking devices with arbitrary shapes. As a target of a cloaking device, the two-dimensional cylindrical cloaking device is chosen as well as 3.1 because ε and μ can be represented by the analytical function, with which we can compare those represented by the

solution of the Laplace's equation based on the FEM with respect to the cloaking performance. The cloaking performance is calculated with five full-mesh resolutions where the average lengths are 2.5, 1.0, 0.5, 0.25, and 0.10 mm. Their relative full-mesh resolutions correspond to 4.17e-02, 1.67e-02, 8.33e-03, 4.17e-03, and 1.67e-03. The surface of the cloaking device is modelled by the mesh representation approach with the same relative mesh resolutions as the relative full-mesh resolution inside of the cloaking device.

The ray paths obtained for the five relative full-mesh resolutions are illustrated in Fig. 10 (a)-(e), respectively, which show that some ray paths deviate from ideal ones for the coarse mesh resolutions. The dependence of the cloaking performance on the relative full-mesh resolution is calculated in Table 2. We can find that the cloaking performance becomes better as the relative full-mesh resolution gets finer. At the relative full-mesh resolution of 1.67e-03, we can obtain the value of $\Delta\theta$ less than 1°. Comparing Table 2 with Table 1, it can be seen that the cloaking performance by the full-mesh representation approach at each relative resolution is lower than that by the analytical function approach at the same relative mesh resolution.

The dependence of the cloaking performance on the radiation angle for the five relative full-mesh resolutions is shown in Fig. 11 (a)-(e), respectively. At the relative full-mesh resolution from 4.17e-02 to 4.17e-03, it can be seen that the performance becomes deteriorated at the radiation angle close to 0.0°, suggesting that this deterioration is caused by the ray passing near the inner boundary. When a ray sufficiently approaches the inner boundary, the ray paths were influenced by $\boldsymbol{\varepsilon}$ and $\boldsymbol{\mu}$ at the inner boundary, which are very large. If the full-mesh resolution is not sufficiently fine, the sampled data of $\boldsymbol{\varepsilon}$ and $\boldsymbol{\mu}$ cannot be represented correctly by the linear interpolation, which causes large error to the ray path.

Since $\boldsymbol{\varepsilon}$ and $\boldsymbol{\mu}$ in the full-mesh representation are represented by the interpolation function using the values of the FEM-based solution, the accuracy in the full-mesh representation can be divided into two types. One type is the accuracy of the FEM, that is, how close the FEM-based solution is to the rigorous solution. The other type is the accuracy of the interpolation, that is, how close the interpolation function is to the rigorous function. Figure 12 shows schematically the two types of accuracies. As the relative full-mesh resolution becomes finer, both of the two accuracies are improved and converged to the rigorous function. At a certain accuracy of the interpolation, the best accuracy of the FEM corresponds to the interpolation using the values of the rigorous solution of the Laplace's equation. Therefore, we can investigate the accuracy of the FEM by comparing cloaking performances for $\boldsymbol{\varepsilon}$ and $\boldsymbol{\mu}$ represented by the linear interpolation of the values of the FEM-based solution and those represented by the linear interpolation of the values of the rigorous solution at the same relative full-mesh resolution, as indicated by the green arrow in Fig. 12.

On the other hand, we can investigate only effects of the accuracy of the interpolation by comparing cloaking performances for the interpolation function using the values of the rigorous function at various relative full-mesh resolutions, as indicated by the blue arrow in Fig. 12, since this function has no error in terms of the accuracy of the FEM.

In order to divide the accuracy into the two types, we calculate the cloaking performance of cylindrical cloaking with five relative full-mesh resolutions, 4.17e-02, 1.67e-02, 8.33e-03, 4.17e-03, and 1.67e-03, by employing $\boldsymbol{\varepsilon}$ and $\boldsymbol{\mu}$ represented by linear interpolations of the values of the rigorous solution of the Laplace's equation. The surface of the cloaking device is modelled by the mesh representation approach with the same relative mesh resolutions as the relative full-mesh resolution inside of the cloaking device.

The ray trajectories obtained from the interpolation of the rigorous solution with the five relative full-mesh resolutions are illustrated in Figs. 13 (a)-(e), respectively. The dependence of the cloaking performance on the radiation angle for the five relative full-mesh resolutions are shown in Figs. 14 (a)-(e), respectively. Comparing Fig. 10 with Fig. 13, or Fig. 11 with Fig. 14, it can be seen that the similar results to the FEM-based solution are obtained. The dependence of the cloaking performance on the relative full-mesh resolution is shown in Table 2. From Table 2, the effect of the interpolation on the accuracy is found to be very large. From Fig. 14, the effect of the interpolation noticeably appears in the small radiation angles, which correspond to the largely deviated ray trajectories depicted in Fig. 13. As described above, if the relative full-mesh resolution is not fine sufficiently, $\boldsymbol{\varepsilon}$ and $\boldsymbol{\mu}$ cannot be modeled accurately by the linear interpolation, resulting in the large error in the ray path.

In order to examine the accuracy of the FEM, we compare the cloaking performance for ε and μ represented by linear interpolations of the FEM-based solution with those for ε and μ represented by linear interpolations of the rigorous solution in Table 2. We can see that the difference between them at each relative full-mesh resolution is very small, which suggests that the accuracy of the FEM gives a smaller effect on the cloaking performance than the accuracy of the interpolation does.

From the above results, we can show that the relative full-mesh resolution inside the cloaking device finer than 1.67e-03 is recommended for the evaluation of cloaking devices with arbitrary shapes.

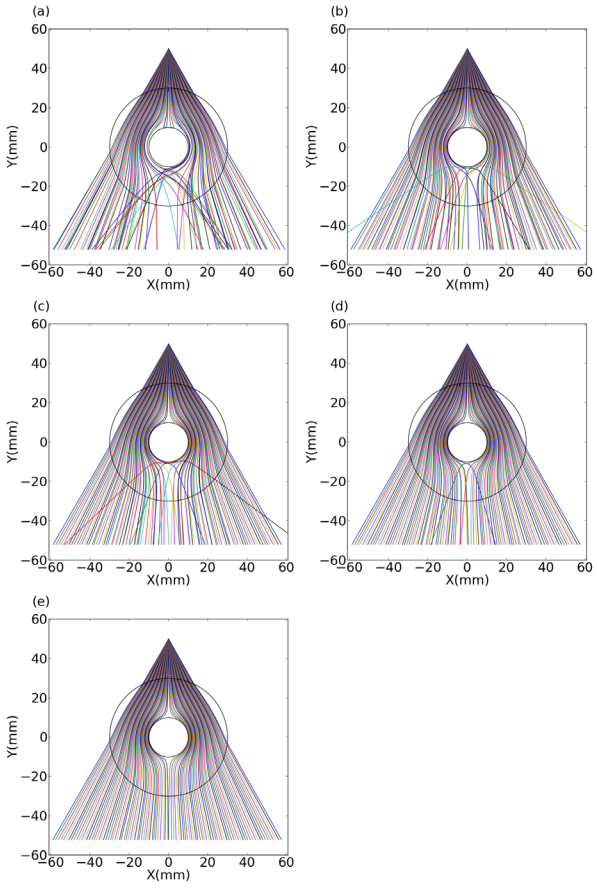

Fig. 10. The ray paths with the cylindrical cloaking device for the mesh representation approach for the surface of the cloaking device and the linear interpolation of the FEM-based solution of the Laplace's equation for $\boldsymbol{\varepsilon}$ and $\boldsymbol{\mu}$ inside of the cloaking device. The relative full-

mesh resolutions are (a) 4.17e-02, (b) 1.67e-02, (c) 8.33e-03, (d) 4.17e-03 and (e) 1.67e-03.

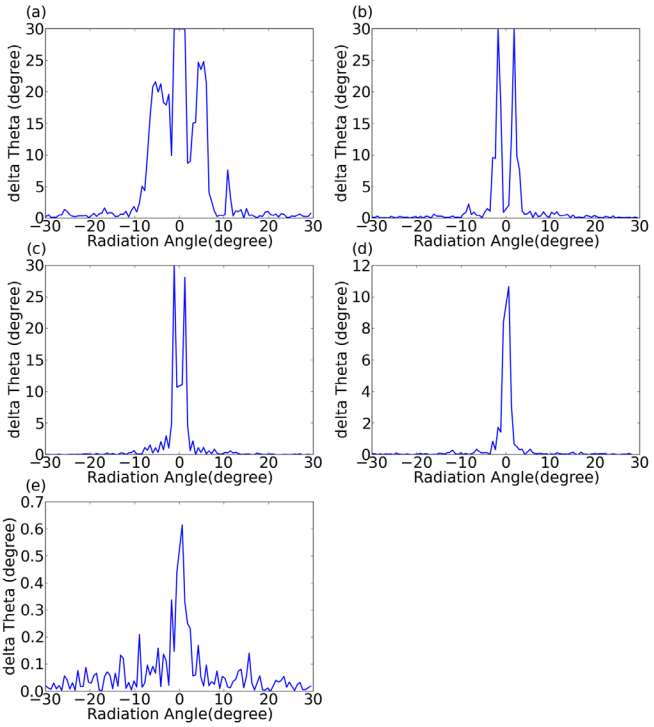

Fig. 11. The dependence of the cloaking performance of the cylindrical cloaking device on the radiation angle for the mesh representation approach for the surface of the cloaking device and the linear interpolation of the FEM-based solution of the Laplace's equation for **ε** and **μ** inside of the cloaking device. The relative full-mesh resolutions are (a) 4.17e-02, (b) 1.67e-02, (c) 8.33e-03, (d) 4.17e-03 and (e) 1.67e-03.

Table 2: Performances of the cylindrical cloaking device calculated for the full-mesh representation with the interpolation of the FEM-based solution of the Laplace's equation and with the interpolation of the rigorous solution of the Laplace's equation

Number	Surface representation		Inside representation		Δθ (°)
1	Mesh	4.17e-02	Full-mesh (FEM based)	4.17e-02	12.1
2		1.67e-02		1.67e-02	5.19
3		8.33e-03		8.33e-03	4.51
4		4.17e-03		4.17e-03	1.43
5		1.67e-03		1.67e-03	0.113
6	Mesh	4.17e-02	Full-mesh (Rigorous)	4.17e-02	11.0
7		1.67e-02		1.67e-02	5.36
8		8.33e-03		8.33e-03	3.62
9		4.17e-03		4.17e-03	1.13
10		1.67e-03		1.67e-03	0.182

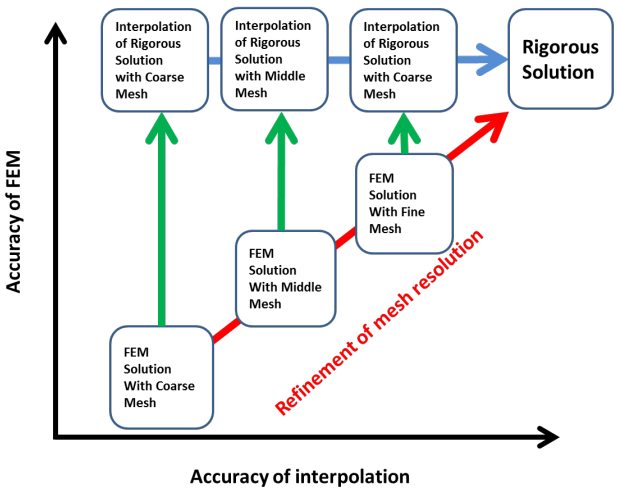

Fig. 12. Two types of accuracy in the full-mesh resolution: the accuracy of the interpolation and the accuracy of the FEM.

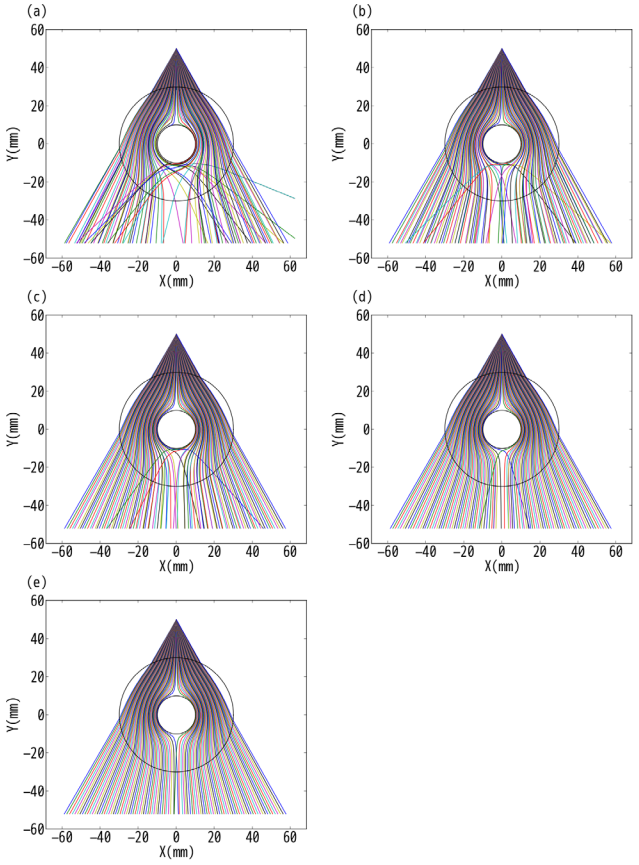

Fig. 13. The ray paths with the cylindrical cloaking device for the mesh representation approach for the surface of the cloaking device and the linear interpolation of the rigorous solution of the Laplace's equation for **ε** and **μ** inside of the cloaking device. The relative full-mesh resolutions are (a) 4.17e-02, (b) 1.67e-02, (c) 8.33e-03, (d) 4.17e-03 and (e) 1.67e-03.

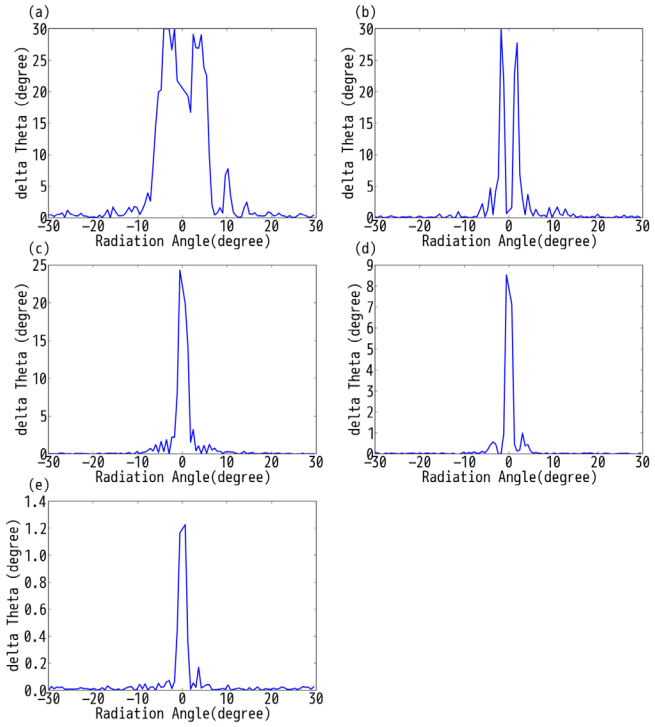

Fig. 14. The dependence of the cloaking performance of the cylindrical cloaking device on the radiation angle for the mesh representation approach for the surface of the cloaking device and t the linear interpolation of the rigorous solution of the Laplace's equation for **ε** and **μ** inside of the cloaking device. The relative full-mesh resolutions are (a) 4.17e-02, (b) 1.67e-02, (c) 8.33e-03, (d) 4.17e-03 and (e) 1.67e-03.

3.3. Analysis of Double Cylindrical Cloaking Device

We analyze the double cylindrical cloaking device as shown in Fig. 15 as an example of arbitrary shapes. From 3.1 and 3.2, we employ the relative mesh resolution of 1.67e-03 for the surface and the relative full-mesh resolution of 1.67e-03 for the inside of the cloaking device. **ε** and **μ** are represented by linear interpolations of the solution of the Laplace's equation based on the FEM. The calculated ray paths are shown in Fig. 16 (a). The performance obtained from the ray paths is $\Delta\theta$ = 0.651, which suggests that the performance for the double cylindrical cloaking device is smaller than that for the cylindrical cloaking device. The dependence of the cloaking performance on the radiation angle is shown in Fig. 16 (b). From Fig. 16 (b), we can find that the performance is deteriorated around the radiation angle of -18°. The radiation angle corresponds to the ray path passing near one of two points where the two cylinders are connected. Therefore, the reason of the lower performance of the double cylindrical cloaking device is considered to be due to the error occurred near the point, which shows singularity in the solution of the FEM. Except for the singular point, nevertheless, it is found that the performance is comparable to that of the cylindrical cloaking device.

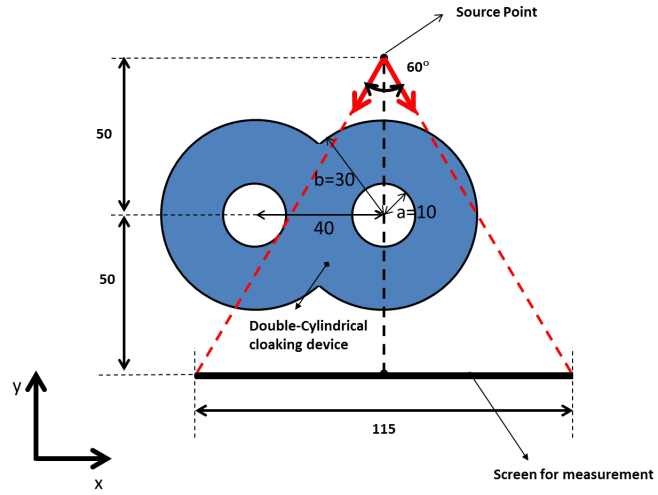

Fig. 15. Calculation model for the double-cylindrical cloaking device

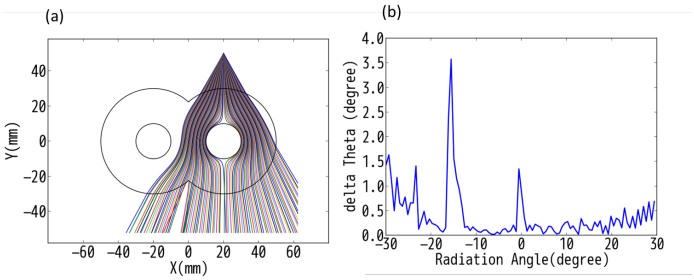

Fig. 16. (a) The ray paths with the double-cylindrical cloaking device. (b) The dependence of the cloaking performance of the double cylindrical cloaking device on the radiation angle.

3.4. Analysis of Huge Arbitrary Cloaking Device

As the other example of cloaking devices with arbitrary shapes, we study the huge cloaking device with the completely arbitrary shape as shown in Fig. 17 [27]. As well as the double cylindrical cloaking device described in 3.3, we employ the relative mesh resolution of 1.67e-03 for the surface and the relative full-mesh resolution of 1.67e-03. The representative length for determining the relative full-mesh resolution is determined to be 6 m from the size of the cloaking device. Therefore, the actual full-mesh resolution corresponds to 0.01 m.

The calculated ray paths are shown in Fig. 18 (a). The dependence of the cloaking performance on the radiation angle is shown in Fig. 19 (a). We can find that the performance is deteriorated at the radiation angle close to 0.0°. The evaluation value of the cloaking device is $\Delta\theta$= 2.54°, which suggests that the performance for the cloaking device is smaller than that for the cylindrical cloaking device. The reason for the deterioration of the performance is considered to be the low accuracy of the interpolation described in 3.2.

Since the accuracy of the interpolation can be improved by refining the full-mesh resolution, we calculate ray trajectories with the relative full-mesh resolution of 8.33e-04. The calculated ray paths and the dependence of the cloaking performance on the radiation angle are shown in Fig. 18 (b) and Fig. 19 (b), respectively. They show that the error of the ray paths becomes smaller at the relative full-mesh resolution of 8.33e-04 than at that of 1.67e-03. Therefore, $\Delta\theta$ at the full-mesh resolution of 8.33e-04 is 0.343° that is smaller than that at the full-mesh resolution of 1.67e-03. From the above results, it can be seen that a finer full-mesh resolution is required for good performance of a

cloaking devices with general shapes than with regular shapes like a cylinder.

Here, we estimate the computational memory and the computational speed for the proposed Hamiltonian-based ray tracing. In the case of the huge cloaking device with the completely arbitrary shape with the full-mesh resolution of 8.33e-04, less than 2.5 GB of memory is required for our Hamiltonian-based ray tracing. If the same model is calculated by full-wave simulation, more than 300 PB of memory is estimated to be required. The usage of such a huge amount of memory is beyond the capacities of current supercomputers. Therefore, in terms of memory usages, the proposed Hamiltonian-based ray tracing is efficient for large-scale objects. On the other hand, it takes approximately 5 hours to obtain ray trajectories by using 5 CPU cores (Intel Xeon E5-2687W 3.1GHz). This calculation speed is much faster than full-wave simulation. If more CPU cores are available in the parallel computation, the computational speed can be faster in proportion to the number of CPU cores, leading to sufficient computational speed for design of large-scale cloaking devices.

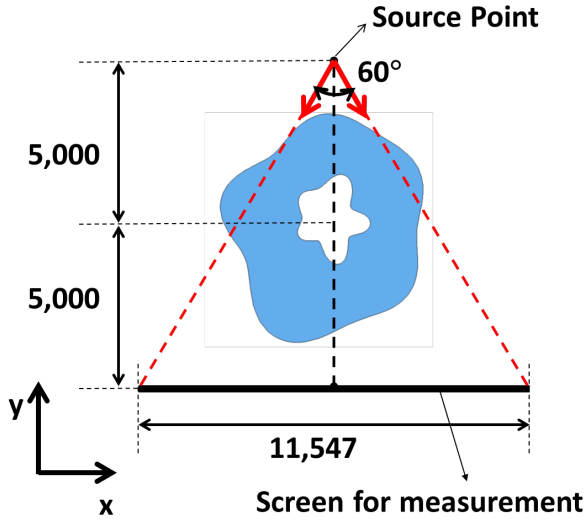

Fig. 17. Calculation model for the huge arbitrary cloaking device.

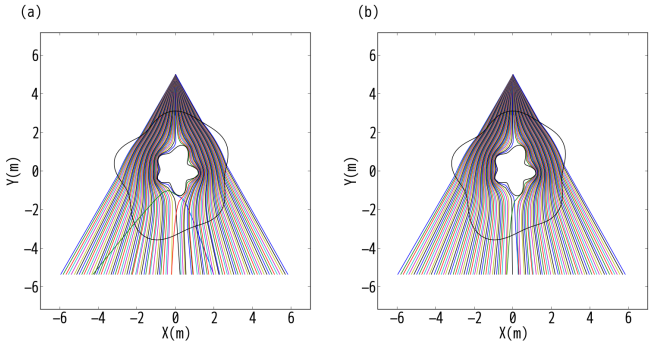

Fig. 18. The ray trajectories with the huge arbitrary cloaking device. The relative full-mesh resolutions are (a) 1.67e-03, (b) 8.33e-04.

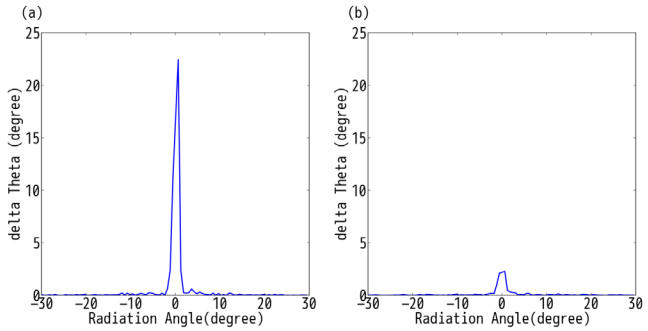

Fig. 19. The dependence of the cloaking performance of the huge arbitrary cloaking device on the radiation angle. The relative full-mesh resolutions are (a) 1.67e-03, (b) 8.33e-04.

4. Conclusion

We have applied our Hamiltonian ray tracing and the full-mesh representation approach to the double cylindrical cloaking device and the huge arbitrary cloaking device as examples of cloaking devices with arbitrary shapes as well as the cylindrical cloaking device. For the calculation of $\boldsymbol{\varepsilon}$ and $\boldsymbol{\mu}$ of these cloaking devices, the numerical method using the solution of the Laplace's equation based on the FEM has been employed.

Based on the obtained results, we can suggest a general guideline for the full-mesh resolution as follows. A relative full-mesh resolution finer than 1.67e-03 is found to be required for good performance in cloaking devices with regular shapes like a cylinder, whereas a relative full-mesh resolution finer than 8.33e-04 is found to be required in cloaking devices with general shapes.

The numerical results of the double cylindrical cloaking device and the huge arbitrary cloaking device have shown good performance. These results suggest that our Hamiltonian ray tracing can be applied to the evaluation of the performance of cloaking devices with arbitrary shapes and the full-mesh representation. The full-mesh representation is also useful to fabricate the actual devices.

Acknowledgements

We are grateful to Mr. Toshiharu Yamamoto and Mr. Masahiro Tsukamoto with AsahiKasei Corp. for their valuable comments and discussion.

Reference

1. J. B. Pendry, D. Schurig, and D. R. Smith, "Controlling electromagnetic fields," Science **312**, 1780–1782 (2006).
2. U. Leonhardt, "Optical conformal mapping," Science **312**, 1777–1780 (2006).
3. D. Schurig, J. J. Mock, B. J. Justice, S. A. Cummer, J. B. Pendry, A. F. Starr, and D. R. Smith, "Metamaterial electromagnetic cloak at microwave frequencies," Science **314**, 977–980 (2006).
4. W. Cai, U. K. Chettiar, A. V. Kildishev, and V. M. Shalaev, "Optical cloaking with non-magnetic metamaterials," Nat. Photonics **1**, 224–227 (2007).
5. D. Gao, C. Qiu, L. Gao, T. Cui, and S. Zhang, "Macroscopic broadband optical escalator with force-loaded transformation optics," Opt. Express **21**, 796–803 (2013).
6. R. Beach, "Killer pillars the blinding truth," http://www.safespeed.org.uk/bike005.pdf.
7. N. Joseph, "Jaguar and Rover develops 'transparent' A-pillar and ghost car," http://www.autoblog.com/2014/12/15/jaguar-land-rover-360-

virtual - urban - windscreen - transparent - pillar - follow - me - ghost - carnavigation - systems - video - official/.
8. T. Yoshida, K. Jo, K. Minamizawa, H. Nii, N. Kawakami, and S. Tachi, Transparent Cockpit: Visual Assistance System for Vehicle Using Retro-Reflective Projection Technology (IEEE, 2008), pp. 185–188.
9. M. Inami, N. Kawakami, and S. Tachi, Optical Camouflage Using Retro-Reflective Projection Technology (IEEE, 2003), pp. 348–349.
10. D. Schurig, J. B. Pendry, and D. R. Smith, "Calculation of material properties and ray tracing in transformation media," Opt. Express **14**, 9794–9804 (2006).
11. M. M. Crosskey, A. T. Nixon, L. M. Schick, and G. Kovačič, "Invisibility cloaking via non-smooth transformation optics and ray tracing," Phys. Lett. A **375**, 1903–1911 (2011).
12. L. M. Zhong, T. M. Niu, J. Bai, and T. J. Cui, "Design of transparent cloaks with arbitrarily inner and outer boundaries," J. Appl. Phys. **107**, 124908 (2010).
13. J. Hu, X. Zhou, and G. Hu, "Nonsingular two dimensional cloak of arbitrary shape," Appl. Phys. Lett. **95**, 011107 (2009).
14. X. Wang, S. Qu, S. Xia, B. Wang, Z. Xu, H. Ma, J. Wang, C. Gu, X. Wu, L. Lu, and H. Zhou, "Numerical methods for three-dimensional electromagnetic invisible cloaks with irregular boundary shapes," in Proceedings of Progress In Electromagnetics Research Symposium, Xi'an, China (2010), pp. 1649–1652.
15. X. Wang, S. Qu, S. Xia, B. Wang, Z. Xu, H. Ma, J. Wang, C. Gu, X. Wu, L. Lu, and H. Zhou, "Numerical method of designing three-dimensional open cloaks with arbitrary boundary shapes," Photon. Nanostr. Fundam. Appl. **8**, 205–208 (2010).
16. X. Wang, S. Qu, Z. Xu, H. Ma, J. Wang, C. Gu, and X. Wu, "Three-dimensional invisible cloaks with arbitrary shapes based on partial differential equation," Appl. Math. Comput. **216**, 426–430 (2010).
17. J. C. Halimeh and M. Wegener, "Photorealistic rendering of unidirectional free-space invisibility cloaks," Opt. Express **21**, 9457–9472 (2013).
18. J. C. Halimeh and M. Wegener, "Time-of-flight imaging of invisibility cloaks," Opt. Express **20**, 63–74 (2012).
19. J. C. Halimeh, R. Schmied, and M. Wegener, "Newtonian photorealistic ray tracing of grating cloaks and correlation-function-based cloaking-quality assessment," Opt. Express **19**, 6078–6092 (2011).
20. J. C. Halimeh and M. Wegener, "Photorealistic ray tracing of freespace invisibility cloaks made of uniaxial dielectrics," Opt. Express **20**, 28330–28340 (2012).
21. A. J. Danner, "Visualizing invisibility: metamaterials-based optical devices in natural environments," Opt. Express **18**, 3332–3337 (2010).
22. G. Dolling, M. Wegener, S. Linden, and C. Hormann, "Photorealistic images of objects in effective negative-index materials," Opt. Express **14**, 1842–1849 (2006).
23. A. Akbarzadeh and A. J. Danner, "Generalization of ray tracing in a linear inhomogeneous anisotropic medium: a coordinate-free approach," J. Opt. Soc. Am. A **27**, 2558-2562 (2010).
24. C. Qiu, A. Akbarzadeh, T. Han, and A. J. Danner, "Photorealistic rendering of a graded negative-index metamaterial magnifier," New J. Phys. **14,** 033024 (2012).
25. A. Akbarzadeh, J. A. Crosse, M. Danesh, C. Qiu, A. J. Danner, and C. M. Soukoulis, "Interplay of Optical Force and Ray-Optic Behavior between Luneburg Lenses," ACS Photonics **2**, 1384−1390 (2015).
26. T. Tanaka and O. Matoba, "Hamiltonian-based ray-tracing method with triangular-mesh representation for a large-scale cloaking device with an arbitrary shape," Appl. Opt. **55**, 3456-3461 (2016).
27. J. Hu, X. Zhou and G. Hu, "Design method for electromagnetic cloak with arbitrary shapes based on Laplace's equation," Opt. Express **17**, 1308-1320 (2009).
28. https://www.csc.fi/web/elmer
29. W. Yan, M. Yan, Z. Ruan, and M. Qiu, "Coordinate transformations make perfect invisibility cloaks with arbitrary shape," New J. Phys. **10,** 043040 (2008).
30. W. X. Jiang, J. Y. Chin, Z. Li, Q. Cheng, R. Liu, and T. J. Cui, "Analytical design of conformally invisible cloaks for arbitrarily shaped objects," Phys. Rev. E **77**, 066607 (2008).
31. H. Ma, S. Qu, Z. Xu, and J. Wang, "Numerical method for designing approximate cloaks with arbitrary shapes," Phys. Rev. E **78**, 036608 (2008).